Monthly Notices of the ROYAL ASTRONOMICAL SOCIETY

MNRAS **505,** 689–701 (2021) doi:10.1093/mnras/stab1303
Advance Access publication 2021 May 10

Constraining the ratio of median pixel optical depth profile around $z \sim 4$ quasars using the longitudinal proximity effect

Priyanka Jalan,[1,2]★ Hum Chand[1,3] and Raghunathan Srianand[4]

[1]*Aryabhatta Research Institute of Observational Sciences (ARIES), Manora Peak, Nainital 263002, India*
[2]*Department of Physics and Astrophysics, University of Delhi, Delhi 110007, India*
[3]*Department of Physics and Astronomical Sciences, Central University of Himachal Pradesh (CUHP), Dharamshala 176215, India*
[4]*Inter-University Centre for Astronomy and Astrophysics (IUCAA), Postbag 4, Ganeshkhind, Pune 411 007, India*

Accepted 2021 May 3. Received 2021 May 3; in original form 2020 July 7

ABSTRACT

We present a detailed study of the longitudinal proximity effect using a sample of 85 quasars spanning an emission redshift range of $3.5 \leq z_{\rm em} \leq 4.5$ and Lyman continuum luminosity (L_{912}) ranging from 1.06×10^{31} to 2.24×10^{32} erg s^{-1} Hz^{-1}. We use the high-quality spectra of these quasars obtained at a spectral resolution of $R \sim 5100$ and S/N ~ 30 using X-SHOOTER spectrograph mounted on the Very Large Telescope (VLT). In our analysis, we compared the transmitted flux and pixel optical depth of the Ly α absorption originating from the vicinity of quasars to those from the general intergalactic medium (IGM) by using a redshift-matched control sample. The longitudinal proximity effect is found up to $r \leq 12$ Mpc (proper) from quasars. By appropriately scaling up the pixel optical depth in the vicinity of quasars to account for the excess ionization by quasars, we constrain the ratio of median H I optical depth in the vicinity of the quasar to that of the IGM ($R_\tau(r)$). The $R_\tau(r)$ is found to be significantly higher than unity up to 6 Mpc from the quasar with a typical radial profile of the form $R_\tau(r) = 1 + A \times \exp(-r/r_0)$ with $A = 9.16 \pm 0.68$ and $r_0 = 1.27 \pm 0.08$ Mpc. The integrated value of the scaled pixel optical depth over the radial bin of 0–6 Mpc is found to be higher by a factor of 2.55 ± 0.17 than the corresponding integrated value of the median pixel optical depth of the IGM. We also found $R_\tau(r)$ to be luminosity dependent.

Key words: galaxies: high-redshift – intergalactic medium – quasars: absorption lines.

1 INTRODUCTION

Previous studies using spectra of distant quasars have established that the number of Ly α forest absorption lines per unit redshift generally increases with increasing redshift (e.g. see Lu, Wolfe & Turnshek 1991; Giallongo 1991; Kulkarni & Fall 1993; Bechtold 1994; Giallongo et al. 1996; Scott et al. 2000; Kim et al. 2007; Dall'Aglio, Wisotzki & Worseck 2008b; Calverley et al. 2011; Partl et al. 2011; Becker et al. 2013; Becker, Bolton & Lidz 2015; Monzon et al. 2020). However, in the vicinity of a quasar (up to several proper Mpc), the ionizing photons from the quasar will dominate the ionization state of the gas over those from the ultraviolet background (UVB) radiation. This produces a region of less Ly α absorption (i.e. enhanced transmitted flux) near the emission redshift ($z_{\rm em}$) of the quasar, first noted by Carswell et al. (1982), known as the *proximity effect* (e.g. see Murdoch et al. 1986; Tytler 1987; Bajtlik, Duncan & Ostriker 1988; Kulkarni & Fall 1993; Bechtold 1994; Srianand & Khare 1996; Cooke, Espey & Carswell 1997; Liske & Williger 2001; Worseck & Wisotzki 2006; Faucher-Giguère et al. 2008a; Wild et al. 2008; Prochaska et al. 2013; Khrykin et al. 2016; Jalan, Chand & Srianand 2019).

The distance up to which the effect of quasar's radiation dominates depends on the intensity of UVB and H I ionizing luminosity of the quasar. Therefore, the proximity effect has been used by many previous studies to get an estimate of the strength of the UVB radiation at various redshifts (e.g. see Bajtlik et al. 1988; Kulkarni & Fall 1993; Giallongo et al. 1996; Cooke et al. 1997; Scott et al. 2000; Liske & Williger 2001; Dall'Aglio et al. 2008b). However, most of these classical proximity effect analyses assume that the density distribution of gas in the vicinity of a quasar is similar to that far away from it, i.e. the general intergalactic medium (IGM; for more details, see also Faucher-Giguère et al. 2008a; Calverley et al. 2011; Partl et al. 2011). This could cause the intensity of the UVB radiation to be overestimated by up to a factor of 2–3 when measured using the proximity effect (Loeb & Eisenstein 1995; Faucher-Giguère et al. 2008a).

However, instead of measuring the UVB intensity from the proximity effect analysis, the procedure can be reversed to estimate the density profile around the quasar (e.g. see Scott et al. 2000; Rollinde et al. 2005; Guimarães et al. 2007; D'Odorico et al. 2008), if the UVB measurements are known from an independent method (Faucher-Giguère et al. 2009; Haardt & Madau 2012; Khaire & Srianand 2015a, 2019, and references therein). Additionally, the gas distribution in the transverse direction of the quasar can be studied using multiple sightlines with small separations. The expected decrement of the Ly α absorption lines in the spectrum of the background quasar near the emission redshift of the foreground quasar induced by the ionizing radiation from the foreground quasar in its transverse direction is known as transverse proximity effect (e.g. see Srianand 1997; Adelberger 2004; Schirber, Miralda-Escudé

★ E-mail: priyajalan14@gmail.com

& McDonald 2004; Rollinde et al. 2005; Worseck et al. 2007; Gonçalves, Steidel & Pettini 2008; Gallerani 2011; Hennawi & Prochaska 2013; Schmidt et al. 2018; Jalan et al. 2019).

In our previous work, Jalan et al. (2019, hereafter, JCS19), we studied the proximity effect in the longitudinal and transverse directions for quasars at $2.5 \leq z \leq 3.5$. We have used 181 quasar pairs with separation of <1.5 arcmin from SDSS-DR12 (for more information, see Pâris et al. 2017) quasar catalogue. Our analysis includes a novel technique of studying the proximity effect using a control sample of quasars, matching in the absorption redshift and continuum signal-to-noise ratio (S/N), to take into account the effect of optical depth evolution with the redshift. We compared the transmitted flux and/or optical depth from Ly α absorption lines originating in the vicinity and far from the quasar, i.e. IGM. We detected enhancement and decrement of the transmitted flux within a radial distance of 4 Mpc from the quasar in the longitudinal and transverse directions, respectively. Additionally, JCS19 has also taken into account the effect of spectral resolution and optical depth while lifting the degeneracy between excess ionization from the quasars and the excess density of the absorbing gas based on their detailed simulations. The ratio of median pixel optical depth in the longitudinal direction after applying the ionization correction is found to be consistent with that in the transverse direction without applying any correction for ionization by the quasars. We interpreted this as an indication for the presence of an anisotropic obscuration in the transverse direction (e.g. by dusty torus) with ≤27 per cent (at 3σ confidence level) quasar's ionization/illumination as compared to its longitudinal direction. We found that our sample was dominated by Type-I AGNs, which supported the results (also see Prochaska, Lau & Hennawi 2014; Lau, Prochaska & Hennawi 2016, 2018).

The main focus of our previous work (JCS19) was to carry out the comparison of the gas distribution around quasars at $<z_{\rm em}> \sim 3$ along the longitudinal and transverse directions. In this paper, we aim to extend our analysis of the longitudinal proximity effect to higher redshifts by applying a similar technique as used in JCS19. However, due to the steep rise in the number of H I clouds with redshifts, the study of longitudinal proximity effect at higher redshift can easily be affected by line blending at a typical spectral resolution of large surveys such as SDSS ($R \sim 2000$). Recently, López, S. et al. (2016) have released a sample of 100 quasars (hereafter, XQ-100 survey) observed with X-SHOOTER spectrograph (e.g. see Vernet et al. 2011) mounted on Very Large Telescope (VLT). Quasars in this sample have $z_{\rm em}$ from 3.5 to 4.71, and the available spectra are of high spectral resolution ($R \sim$ 5000–9000) and high S/N (median ∼30). The advantage of this sample is that due to the large spectral coverage of the X-SHOOTER spectrograph, it is possible to observe Mg II, [O III], and [O II] emission lines that are redshifted to the NIR region for quasars at these redshifts. These emission lines can be used to compute the systemic redshift of the quasars. Thus, the systemic redshifts can be estimated with higher accuracy corresponding to velocity dispersion of <60 km s^{-1} ($\Delta v = c \times \Delta z/[1 + z]$). This accuracy is much higher in comparison to the accuracy achieved using the emission lines lying in the optical region for these quasars. As pointed out by Shen et al. (2016), redshift measured using C III], He II, C IV (after correcting for the luminosity-dependent blueshift), and Mg II lines has the systemic velocity shift of ∼230 km s^{-1}, −167 km s^{-1}, −27 km s^{-1}, and −57 km s^{-1}, and scatter of ∼233 km s^{-1}, 242 km s^{-1}, 415 km s^{-1}, and 205 km s^{-1}, respectively (see also Denney et al. 2016; Eilers et al. 2017; Dix et al. 2020). Therefore, the availability of the high-quality spectra provided by XQ-100 survey at $z_{\rm em} > 3.5$ in conjunction to the aforementioned new technique devised by JCS19 motivates our analysis to estimate the radial profile of the median pixel optical depth around these high-z quasars in comparison to the median pixel optical depth of the general IGM.

The paper is structured as follows. In Section 2, we discuss our sample and its properties. In Section 3, we present transmitted flux analysis and results. This is followed by estimating an appropriate ionization correction using simulated spectra for the pixel optical depth values when observed using a moderate-resolution spectrograph. This relation is then applied to the real data to constrain the median pixel optical depth radial profile around high-z quasars. The discussions and conclusions are presented in Section 4. Throughout this paper, we have used a flat background cosmology with cosmological parameters $\Omega_{\rm m}$, Ω_{λ}, and $H_{\rm o}$ to be 0.286, 0.714, and 69.6 km s^{-1} Mpc^{-1}, respectively, (Bennett et al. 2014). Moreover, all the distances mentioned in this paper are proper distances unless noted otherwise.

2 DATA AND ITS PROPERTIES

We use 100 quasar spectra from the XQ-100 survey, obtained using VLT/X-SHOOTER in the period between 2012 February 10 and 2014 February 23 within the ESO large program titled 'Quasars and their absorption lines: a legacy survey of the high redshift universe with X-SHOOTER' led by López, S. et al. (2016). X-SHOOTER is a triple-arm spectrograph, with UV-Blue,[1] VIS (visible), and NIR (near-infrared) arm covering a spectral range of 315–560 nm, 540–1020 nm, and 1000–2480 nm (e.g. see also Vernet et al. 2011), respectively. Therefore, in one integration, X-SHOOTER provides a spectral coverage from ∼310 nm (atmospheric cutoff) to 2480 nm (NIR) at a moderate resolution of $R \approx$ 5000–9000. The coverage up to 2480 nm is available only for 47 of the quasars in the sample due to the employed *K*-band blocking filter. However, this spectral coverage leads to the full coverage of the Ly α forest in the optical spectral regime for the quasars at higher redshifts, and the [O III], [O II], and Mg II emission lines in the NIR regime allow one to have a precise estimate of systemic redshifts of the quasars (e.g. see Section 3.2). The distribution of emission redshifts of these 100 quasars spanning a range of 3.51–4.71 is shown in Fig. 1. These are measured using principal component analysis (PCA). The details of the sample are fully described in López, S. et al. (2016).

For the analysis presented here, we mostly utilize the spectra taken in VIS and UV-Blue arms only. The resolving power in the UV-Blue and VIS arm is 5100 (pixel width of 20 km s^{-1}) and 8800 (pixel width of 11 km s^{-1}), respectively, obtained from the header of the fits file and data release, which is also consistent with the findings by Walther et al. (2018). In order to have a similar resolution throughout the spectra, we have convolved the higher resolution spectra of VIS arm to a lower resolution value corresponding to the UV-Blue arm by using a Gaussian kernel with FWHM $= [{\rm FWHM}^2_{\rm UVB} - {\rm FWHM}^2_{\rm VIS}]^{1/2}$. We then interpolated flux, continuum, and error to a common wavelength grid of 20 km s^{-1} per pixel using the 'cubic-spline interpolation method'.

Therefore, the full spectral coverage of the Ly α forest along with the high S/N (median $S/N = 30$) and high resolution ($R \sim 5100$) achieved clearly makes XQ-100 a unique data set to study the quasars proximity effect at high-z. Out of these 100 quasars, we could make use of 85 quasars as the main sample that are marked as flag = 1 in Table 1. The remaining 15 quasars (marked as flag = 0) were

[1]To avoid confusion with UVB as used for ultraviolet background, the UV-blue arm is represented as UV-Blue.

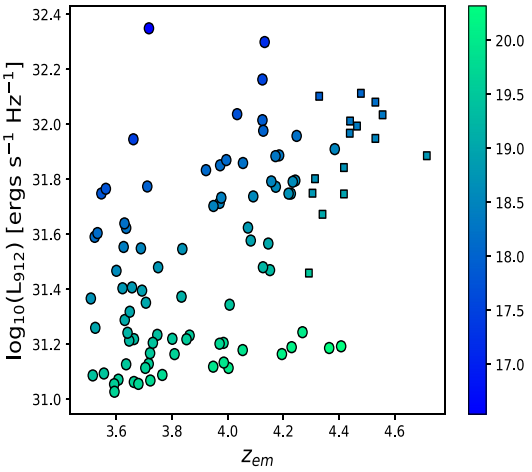

Figure 1. The plot shows the Lyman continuum luminosity (L_{912}) versus emission redshift ($z_{\rm em}$) for the 100 quasars. The colour shade in the right side provides the *V*-band magnitude scale. The circle represents the 85 quasars used in our main sample (see Section 2). The square represents 15 quasars that got excluded from our proximity analysis sample due to lack of control sample, but they are used for the control sample (as elaborated in Section 2.2).

excluded from the proximity sample due to lack of IGM control sample for them but included in the control sample as discussed in Section 2.2 and marked by squares in Fig. 1.

2.1 Distances and luminosities

The Lyman continuum luminosity can be calculated using flux-calibrated spectra as detailed in JCS19. However, as mentioned by López et al. (2016) that the flux values in XQ-100 can be uncertain by an order of magnitude. Therefore, the Lyman continuum luminosity was calculated using the *V*-band magnitude of these quasars based on the formalism provided by Liske & Williger (2001). Here, we assume the continuum to be a power law, i.e. $f_\nu \propto \nu^{-\alpha}$ with the flux density f_ν at the observed wavelength λ as,

$$f_\nu(\lambda) = \left[\frac{\lambda_{\rm V}}{\lambda(1+z_{\rm em})^{-1}}\right]^{-\alpha} (1+z_{\rm em}) \times 10^{-0.4(m_{\rm V}-k_{\rm V})} f_{\nu{\rm V}}(0),$$

where $\lambda_{\rm V}$, $k_{\rm V}$, $m_{\rm V}$ and $f_{\nu{\rm V}}(0)$ are the central wavelength, *K*-correction (e.g. see Cristiani & Vio 1990), observed magnitude, and 0-magnitude flux in the *V*-band respectively. Here, we have assumed

$$\alpha \approx \begin{cases} 0.44; & \lambda > 1300 \text{ Å} \\ 1.57; & \lambda \leq 1300 \text{ Å} \end{cases} \quad (1)$$

(e.g. see Vanden Berk et al. 2001; Telfer et al. 2002; Khaire & Srianand 2015b, and references therein). We note here that the UV-spectral index may vary from quasar to quasar and the impact of ignoring such dispersion was studied in our previous work (JCS19). We found that the effect of this variation is negligible as far as the recovered ratio of median pixel optical depth profile is concerned. Therefore, we have used the value of α as given in equation (1).

We also correct the observed flux value in our spectrum for Galactic extinction (e.g. see Schlegel, Finkbeiner & Davis 1998) by applying a correction factor $10^{0.4A(\lambda)}$ where

$$A(\lambda) = R_{\rm V} E(B-V) \frac{A(\lambda)}{A(V)} \quad (2)$$

using $R_{\rm V} = 3.1$ (e.g. see Clayton & Cardelli 1988; Liske & Williger 2001, and references therein). The flux is calculated at the threshold wavelength of the H I ionizing photons (i.e. 912 Å) and the corresponding luminosity as $4\pi d_L^2 \times F_\nu(912\text{ Å})$, where $d_{\rm L}$ is the luminosity distance to the quasar. As a consistency check of the estimated Lyman continuum luminosity (L_{912}) based on this method, we also used the spectroscopic measurements to calculate it for the 53 sources for which SDSS flux-calibrated spectra are also available. Here, we used the flux at 1325 Å (in the rest frame of quasars) in conjunction with the spectral slope given by equation (1) to compute the F_ν(912 Å) as detailed in JCS19. The same spectra are also used to estimate the *V*-band magnitude using the transfer function as given by Johnson & Morgan (1951). The Lyman continuum luminosity estimated using the spectrum and *V*-band magnitude is found to be consistent with each other within 10 per cent. Therefore, for the sake of homogeneity, we have adopted the L_{912} estimate based on the photometric method for all the sources in our sample. Here, a small caveat could be the difference in the epochs of photometric and spectroscopic observations over which the quasar's magnitude might have varied. For instance, the photometric light curve available in Catalina Real-time Transient Survey (CRTS,[2] Drake et al. 2009) for 96 sources in our sample, observed over a period of about 8 yr, shows a typical variation of ∼10 per cent in their magnitude. This could at the maximum lead to additional 10 per cent uncertainty in the estimated Lyman continuum luminosity.

In Fig. 1, we show $z_{\rm em}$ versus L_{912} for the quasars in our sample along with their *V*-band magnitude (taken from the summary file provided by López et al. 2016). It can be seen from the figure that for our sample, the L_{912} ranges from 1.06×10^{31} to 2.24×10^{32} erg s^{-1} Hz^{-1} and $z_{\rm em}$ in the range from 3.51 to 4.71 (e.g. see Table 1).

The proper radial distance (r) between the quasar with an emission redshift of $z_{\rm em}$ and an absorbing cloud at an absorption redshift of $z_{\rm a}$, is computed as,

$$r(z_{\rm em}, z_{\rm a}) = \frac{c \times [z_{\rm a} - z_{\rm em}]}{(1+z_{\rm em})\, H(z_{\rm em})} = \frac{\Delta\, v}{H(z_{\rm em})}, \quad (3)$$

where $H(z_{\rm em}) = H_0\sqrt{\Omega_{\rm m}(1+z_{\rm em})^3 + \Omega_\lambda}$ is the Hubble constant at $z_{\rm em}$ (Kirkman & Tytler 2008). For further analysis of longitudinal proximity effect, we consider the Ly α forest within -50 Mpc $\leq r(z_{\rm em}, z_{\rm a}) \leq 0$ Mpc along the line of sight to the quasar as the proximity region. The Ly α absorption seen between the Ly β and Ly α emission lines after excluding the proximity region is considered as the IGM in our study. The negative values of the distances given by equation (3) for $z_{\rm a} < z_{\rm em}$ are just to indicate that absorbing clouds are towards the observers. However, in our calculations, we have used the absolute values for distances.

2.2 Control sample of Ly α forest

In this paper, we carry out a statistical analysis by using the transmitted flux ($F_{\rm t}[\lambda_i]$) and pixel optical depth, $\tau(\lambda_i)$ of the Ly α absorption (e.g. see JCS19 and references therein), i.e.

$$F_{\rm t}(\lambda_i) \equiv F(\lambda_i)/F_{\rm c}(\lambda_i) = e^{-\tau(\lambda_i)}, \quad (4)$$

where $\tau(\lambda_i)$ is the pixel optical depth integrated over the pixel width of the observed spectrum (i.e. 20 km s^{-1}). Here, $F(\lambda_i)$ and $F_{\rm c}(\lambda_i)$ are the observed flux and the unabsorbed continuum flux, respectively, at the $i^{\rm th}$ pixel having a wavelength λ_i. In our analysis, the pixels with $F_{\rm t}(\lambda_i) \geq 1$ and $F_{\rm t}(\lambda_i) \leq 0$ are also included. However, since the optical depth values for $F_{\rm t}(\lambda_i) \leq 0$ are ill-defined, we assign $F_{\rm t}(\lambda_i) = \sigma(\lambda_i)$ for such pixels, where $\sigma(\lambda_i)$ represents the

[2] http://crts.caltech.edu

Table 1. Some properties of 100 quasars used in our analysis with masked absorption redshifts.

SN.	Quasar name	z_{em}	Ra (deg)	Dec (deg)	m_V	$\log(L_{912})$ (erg s^{-1} Hz^{-1})	Flag for main sample = 1 for 85 quasars	z_a (class) Masked absorbers in the Ly α forest
(1)	(2)	(3)	(4)	(5)	(6)	(7)	(8)	(9)
1	J0003-2603	4.125	0.845	− 26.055	17.530	32.163	1	3.39 (DLA), 3.39 (NAL SiIV])
2	J0006-6208	4.440	1.715	− 62.134	18.290	32.012	0	3.78 (DLA)
3	J0030-5129	4.173	7.644	− 51.495	18.570	31.773	1	–
4	J0042-1020	3.863	10.582	− 10.337	19.530	31.232	1	–
5	J0048-2442	4.083	12.143	− 24.702	18.940	31.577	1	3.76 (sub-DLA)
..	.....	.....	.....	.....	.....	.....	.....	... ...

Note. Here, we show only a small portion of the table to display its form and contents. The entire table with details of all 100 quasars are available in an online version.

corresponding flux measurement error. Moreover, the percentage of such pixels is very small ($\sim$ 1 per cent); therefore, the inclusion and/or exclusion of these pixels will have a negligible effect on our further analysis. We statistically compare the distribution of the pixel optical depth and/or transmitted flux among the proximity region with that originating from the general IGM. However, in order to combine these values from various absorption redshifts, one has to account for the strong redshift evolution of the optical depth. The evolution curve in principle allows one to scale the optical depth at various absorption redshifts in the proximity region to a reference redshift and then carry out the statistical comparison of it with that of the average optical depth in the IGM at that reference redshift (e.g. see Rollinde et al. 2005; Kirkman & Tytler 2008). However, this method does have a caveat that it may introduce optical depth values by scaling up the continuum noises.

Therefore, instead of using this optical depth evolution curve to scale the optical depths at various redshifts to a reference redshift, we adopt an approach similar to JCS19 of using a control sample. In this regard, we construct a control sample for each proximity region of a spectrum, consisting of those quasars in which their IGM (i.e. $r(z_{em}, z_a) < -50$ Mpc) covers the same Ly α absorption redshift region as that of the proximity region. The method has an advantage as it allows direct comparison of the observed optical depths in the proximity region and IGM region without using any scaling relationships. For constructing such a control sample, we made use of the Ly α forest more than 50 Mpc away from our parent sample of 100 quasars. Out of the 100 main sightlines, we could not find a control sample for seven sightlines with the aforementioned exact match in the redshift. This reduces our main sample to 93 sightlines.

In our search for the control sample, we noticed that for all quasars in our sample, we could get typically about five sightlines of IGM. However, for a few of these sources, we could even get >5 sightlines in the control sample. For such cases, we picked up five sightlines having the closest match in S/N with the Ly α forest in the proximity region. This also helps to ensure a good match in S/N as shown in the top panel of Fig. 2. Also, in the bottom panel of Fig. 2, we show the distribution of relative change of S/N of the proximity region (S/N_p) and IGM region (S/N_{IGM}[3]), i.e. $[\Delta S/N]/[S/N]$ ($\equiv [S/N_p – S/N_{IGM}]/[S/N_p]$) showing a $\leq$25 per cent deviation for about 68 per cent of our sample. For 8 quasars, we could not find a control sample with $|[\Delta S/N]/[S/N]| < 1$ and hence were excluded from our proximity analysis sample. This reduces our main sample from 93 sightlines to 85 sightlines. These 85 quasars are marked with flag = 1 in column 8 of Table 1.

[3]We assign 'p' and 'igm' as subscripts or superscripts to represent the proximity sample and IGM sample, respectively, throughout this paper.

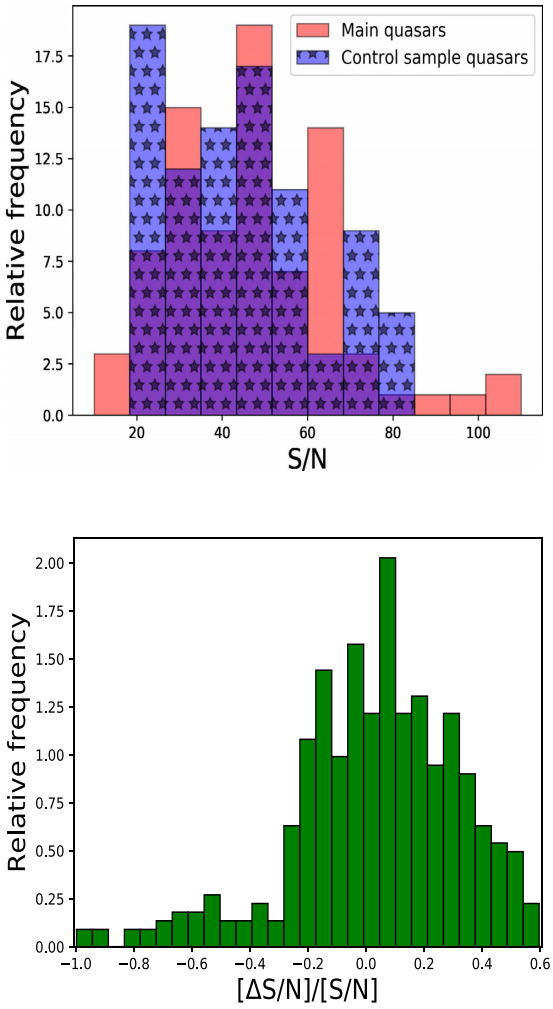

Figure 2. *Top panel*: The histogram plot showing the distribution of the S/N (⟨continuum/error⟩) in the proximity region of the main quasars (S/N_p) and in the corresponding redshift region in the control sample (S/N_{IGM}). The control sample histogram is normalized to that of the peak value of the main quasar's histogram. *Bottom panel*: The histogram plot showing the distribution of $[\Delta S/N]/[S/N]$ ($\equiv [S/N_p – S/N_{IGM}]/[S/N_p]$).

In the lower panel of Fig. 3, we show for illustration a spectrum used as a control sample, and the same for the main sample is shown in the upper panel. It shows the absorption redshift match between the two samples (green dots) with IGM being 50 Mpc away from the quasar's emission. Additionally, all the samples used in our analysis

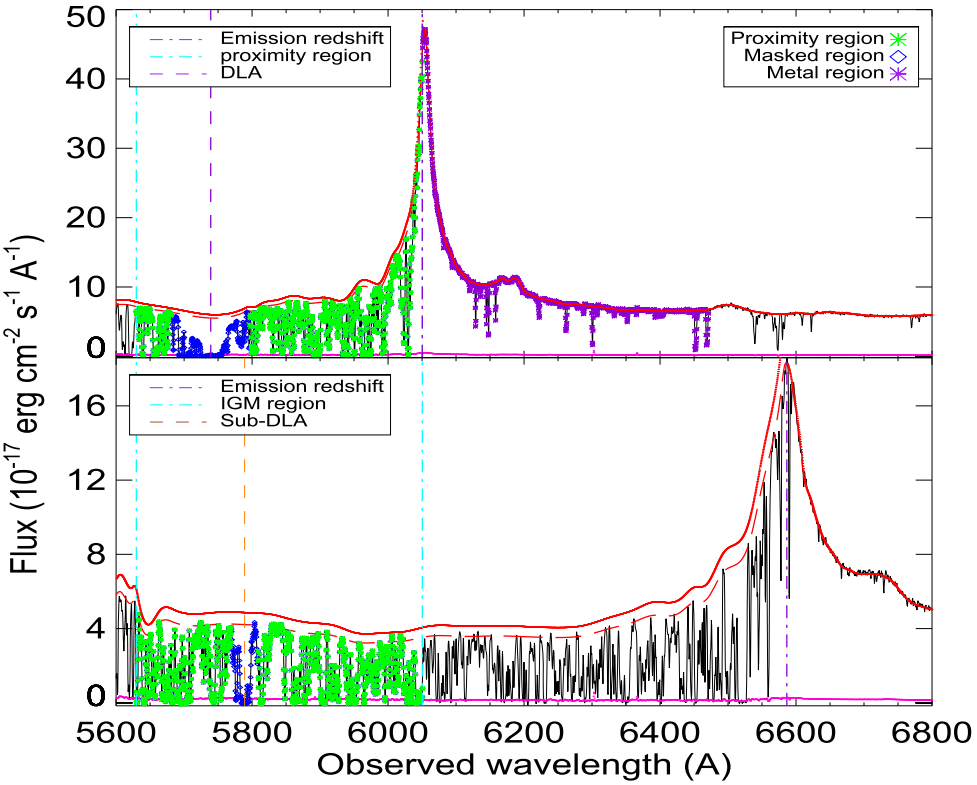

Figure 3. *Upper panel*: Spectrum of one of the quasars (J021429.4-051745.4) at z_{em} =3.977 (purple, dot–dashed vertical line shows the Ly α emission) in our sample. The dashed and solid red curve shows the unabsorbed continuum flux before and after applying the continuum correction, respectively (e.g. see Section 3.1). The vertical dashed lines (cyan) represent the 50-Mpc proximity region. The noise spectrum is also plotted (solid magenta). After masking the $\pm$3000 km s^{-1} region around the absorption redshift of the DLA (purple–dashed line), the pixels considered in the proximity region are shown in dots (green). The purple asterisk sign shows 50-Mpc region redward of the Ly α emission line. *Lower panel*: The plot shows the spectrum of one of the quasars (J052915.9-352601.2) in the corresponding control sample of the above main quasar (e.g. see Section 2.2). The purple dot–dashed line shows the Ly α emission while the cyan-dashed line shows its IGM region corresponding to the above proximity region. After masking the $\pm$1000 km s^{-1} region around the absorption redshift of the sub-DLA (brown–dashed line), the pixels considered in the IGM region are shown in dots (green).

were observed with the same spectral setting in X-SHOOTER. As a result, any effect of spectral resolution will have either a similar or no effect in both of the samples and hence will have minimal impact (if any) for our further analysis.

2.3 DLA, sub-DLA, and NAL

The proximity effect analysis depends on the H I content in the neighbourhood of the quasar as compared to that of the IGM. Therefore, we mask the spectral region consisting of systems such as damped Ly α (DLA)/sub-DLA, narrow-absorption lines (NAL), and Lyman limit systems (LLS) simply to avoid bias due to any strong absorption in our analysis.

To mask such absorption region, we have used Sánchez-Ramírez et al. (2016) compilation, where they have provided a sample of 24 intervening DLA systems and one proximate DLA system with column density (in units of cm^{-2}) log[$N_{\rm H\,I}$] > 20.3 towards these 85 quasars. Similarly, Berg et al. (2019) provide a list of 207 H I absorbers with log[$N_{\rm H\,I}$] > 18.8 along these 85 quasars. Out of these 207 systems, 90 are LLS with 18.8 $\leq$ log[$N_{\rm H\,I}$] $\leq$ 19, 88 are sub-DLAs with 19 < log[$N_{\rm H\,I}$] $\leq$ 20.3, and 22 are identified as DLAs (already included in Sánchez-Ramírez et al. 2016). In these catalogues, they have provided details such as absorption redshifts ($z_{\rm a}$) and column densities of individual systems. We have used the $z_{\rm a}$ information to mask a spectral region of $\pm$ 3000 km s^{-1} and $\pm$1000 km s^{-1} around the absorption redshift of the DLAs and LLS/sub-DLAs, respectively. Additionally, Perrotta et al. (2016) listed the absorption redshift of the 833 NALs consisting of metal absorptions along the 85 quasars in our sample. The Ly α absorption corresponding to these absorbers might be optically thin and hence can respond to the quasar's radiation (e.g. see Kim et al. 2016). Therefore, even though we do not mask the Ly α region, however, if the corresponding metal lines such as C IV, Si IV, N V, and C II lie in the spectral region used in our analysis, we do mask a region of $\pm$500 km s^{-1} around these metal absorption lines. In Fig. 3, we have marked for illustration the masked region in the proximity region of the main sample (top panel) and IGM region of the control sample (bottom panel).

3 ANALYSIS

3.1 Quasar continuum

As evident from equation (4), the analysis of the transmitted flux and the pixel optical depth can be significantly affected by any uncertainty in the continuum fit to the spectral region of the Ly α forest. For the sample of XQ-100 quasar, López et al. (2016) have given the continuum fit based on the cubic spline method as shown with a red-dashed line in Fig. 3. However, as pointed out by Lidz et al. (2006), such an algorithm has its caveat of underestimating

continuum flux in the Ly α forest at low resolution with low S/N data and a careful visual check is required for each spectrum. Additionally, the continuum flux in the Ly α forest at these redshifts, in general, might be underestimated due to the blending of multiple low optical depth Ly α absorption lines (e.g. see also Seljak, McDonald & Makarov 2003; Lidz et al. 2006; Faucher-Giguère et al. 2008a). Therefore, we carried out a visual check of their continuum in the regions that are free from absorption and found that the rms of the fit is better than the 1/[S/N] allowed variation. We note here that such an underestimation of continuum flux will lead to underestimation of the optical depth both in the proximity and in the IGM region (though the uncertainty can be larger in the wings of the Ly α emission line). However, its impact will be slightly diluted at least for the analysis of the ratio of median values of these observed pixel optical depth.

Ideally, it would be better to have mock spectra for these quasars with a known continuum and then fitting the continuum to those mock spectra to get the statistical and systematical continuum uncertainty. In the absence of mock spectra for our data set, we have adopted a conservative estimate of about 10 per cent for statistical continuum uncertainty (per pixel), based on the detailed analysis carried out in JCS19 using mock spectra for SDSS spectra (with known continuum). This is a conservative estimate for the high-quality spectra used here with S/N $\sim$ 20 and $R \sim 5100$. However, for the correction of systematic uncertainty due to the systematic underestimation of continuum, we adopted a typical estimate given by Faucher-Giguère et al. (2008b) as $\Delta C/C_{\rm true} = 1.58 \times 10^{-5}(1 + z)^{5.63}$, where ΔC is the difference between the estimated continuum ($C_{\rm est}$) and actual continuum ($C_{\rm true}$). The analysis was performed using mock spectra with spectral properties similar to that of the data used here. A similar continuum correction is also given by JCS19 for SDSS data and by Becker, Rauch & Sargent (2007) for HIRES data. We present our results using the continuum fits given by López et al. (2016) (e.g. see the red-dashed line in Fig. 3) after applying the aforementioned correction for systematic shift in the continuum (e.g. see the red solid line in Fig. 3). However, for the sake of completeness, we also discuss our results without applying this continuum shift in Section 4.

3.2 Estimation of quasar's emission redshift

An accurate estimation of the emission redshifts for the quasars is a very crucial aspect for the analysis of the proximity effect. For our entire sample, López et al. (2016) have given the $z_{\rm em}$, using their robust method based on PCA. Alternatively, as pointed out by many previous studies (e.g. see Shen et al. 2016, and references therein), [O III] emission line is also a reliable estimator of $z_{\rm em}$, which is covered in spectra of $\sim$45 sources in our sample. We limit the redshift estimation only to 23 quasars (out of 45 quasars), which has strong enough [O III] emission lines (equivalent width, EW $>$ 0.3 Å). Therefore, as a quality check, we fit the doublet of the [O III] lines ($\sim$4959, 5007 Å) for these 23 sources with double Gaussian to fit both broad and narrow components. Furthermore, to make the fit physical, we have tied the values of redshifts and full width at half-maximum (FWHMs) of the doublet lines to have the same values and the intensity ratio to be as 1:3 (i.e. $I_{5007} = 3 \times I_{4959}$) as expected theoretically. We also applied the systemic redshift offset of 48 km s^{-1} as given by Shen et al. (2016) where they assume that Ca II emission line provides the most reliable systemic redshift. We found that our emission redshift estimate is consistent within a typical dispersion of $\sim$150 km s^{-1} with negligible systemic offset with the emission redshifts given by López et al. (2016) estimated using PCA.

Additionally, we also used Mg II emission line, available for all sources to estimate the redshifts, though the line strength was not high enough (i.e. EW $>$ 0.3) for 23 sources (out of 100). After using double Gaussian fit for these 77 sources and applying a systemic redshift offset of 57 km s^{-1} as given by Shen et al. (2016), we again found a negligible systemic difference while comparing with PCA-based redshifts estimates by López et al. (2016). However, we do find a dispersion of $\sim$600 km s^{-1} between redshift estimated using Mg II emission line and PCA-based method (see also Pâris et al. 2017). This suggests that the $z_{\rm em}$ estimated by López et al. (2016) based on the PCA method is in general consistent with [O III] and Mg II emission lines. Finally, for the sake of homogeneity, we have used the $z_{\rm em}$ value as given by López et al. (2016) for the entire sample. However, to be on the conservative side, we have included a dispersion of 600 km s^{-1} as a typical uncertainty in the individual measured emission redshift value in our further analysis.

Additionally, we calculate the statistical uncertainty in the emission redshift using the Monte Carlo simulations. For this, at each pixel with wavelength λ_i, we have generated flux using Gaussian random distribution with a mean value taken as the observed flux (F_i) and width of the distribution as the observed error on F_i. We then estimated the redshift for about 1000 simulated realizations of our sample and found a spread of just 5 km s^{-1}, which is negligible in comparison to the above redshift uncertainty of 600 km s^{-1}.

3.3 Transmitted flux uncertainties

For estimating the uncertainties in the transmitted flux measurements, we follow a similar procedure as detailed in JCS19 with a brief description below. The first contribution of error in the normalized spectrum is propagated from the flux measurement errors and continuum fitting error ($\Delta F_{\rm t}^{\rm fc}[\lambda_i]$) at each pixel. As mentioned in Section 3.1, we have assumed a maximum possible uncertainty of 10 per cent in each pixel as continuum uncertainty as a conservative estimate. It may be noted that there might be a correlation in the continuum placement error within a spectrum. Therefore, the flux error is averaged over the number of pixels in a radial bin w.r.t. the quasars; however, continuum placement error is averaged over the number of spectra contributing in that radial distance bin. This leads to an average of $\Delta F_{\rm t}^{\rm fc}$ value in each radial distance bin. The second contribution to the error in the normalized flux comes from the rms scatter of the normalized flux ($\Delta F_{\rm t}^{\rm rms}$) within each 2-Mpc radial distance bins.

Additionally, we include the uncertainty in the median $F_{\rm t}$ measured in the proximity region due to the typical emission redshift uncertainty ($\Delta F_{\rm t}^{z}$) of $\sim$600 km s^{-1} along our sightlines as discussed in Section 3.2. To calculate this, we add a random (Gaussian generator with σ = 600 km s^{-1}) velocity offset to each quasar emission redshift within $\pm$ 600 km s^{-1} range. The distribution of the median transmitted flux computed for 100 such realizations in a radial bin of 2 Mpc is found to be Gaussian with a width of $\Delta F_{\rm t}^{z}$. Additionally, we also added the sightline-to-sightline variance of the proximity sample ($\Delta F_{\rm t}^{\rm var}$). Here, we used the bootstrap technique (e.g. see Efron & Tibshirani 1993) by the random exclusion of sightlines at the cost of repeating other sightlines. We use 100 such realizations to estimate the width of the Gaussian distribution of the median transmitted flux, $\Delta F_{\rm t}^{\rm var}$, within each 2-Mpc radial distance bins.

Therefore, the total error on the measured transmitted flux in the proximity region ($\Delta F_{\rm t}^{\rm p}$) is given by the quadratic sum of all the above-mentioned errors leading to $\Delta F_{\rm t}^{\rm p}$ for a given 2-Mpc radial

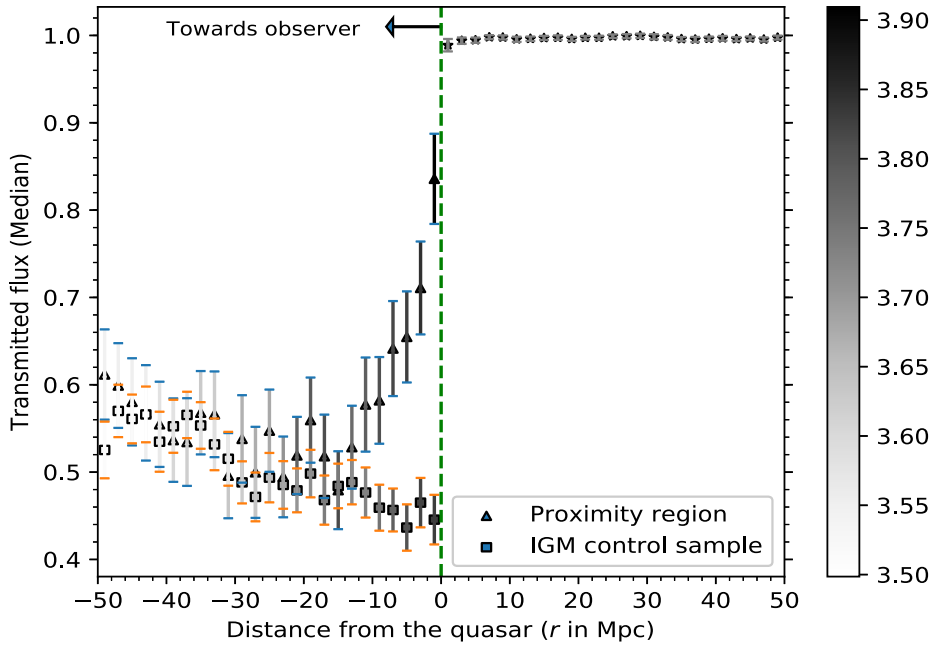

Figure 4. The plot shows the median value of the transmitted flux in various 2-Mpc radial distance bins from the quasars for the proximity region (triangle) and the corresponding control sample (square). The negative distances in the x-axis are just sign convention used in equation (3) to represent the absorbing clouds present in the vicinity of the main quasars towards the observers. The grey shades represent the median value of the absorption redshifts of pixels used in each radial bin. The transmitted flux beyond Ly α emission line is shown with an asterisk sign (without grey shades according to redshift) to distinguish them from the absorption in the Ly α forest. The error bars on the median transmitted flux of the proximity region consist of redshift uncertainty, flux and continuum measurement errors, sightline-to-sightline variance, and rms statistical errors within each radial distance bin [e.g. see equation (5) and/or Section 3.3]. The error bars in the control sample are small due to the large sample size (being ∼5 IGM sightlines per main quasar sightline). The green vertical dashed line shows the location of the main quasars.

distance bin, as,

$$\Delta F_{\rm t}^{\rm p} = \sqrt{\left(\Delta F_{\rm t}^{\rm fc}\right)^2 + \left(\Delta F_{\rm t}^{\rm rms}\right)^2 + \left(\Delta F_{\rm t}^{z}\right)^2 + \left(\Delta F_{\rm t}^{\rm var}\right)^2}. \quad (5)$$

Here, $\Delta F_{\rm t}^{\rm fc}$ is of the order of ∼0.05, $\Delta F_{\rm t}^{\rm rms}$ contributes ∼0.006, and $\Delta F_{\rm t}^{z}$ leads to approximately ∼0.001. Lastly, the $\Delta F_{\rm t}^{\rm var}$ is of the order of ∼0.03 in the Ly α forest. Therefore, the total error is found to be of the order of ∼0.05 in the proximity region within each 2-Mpc radial distance bins.

We follow similar error analysis for the estimation of errors for the control sample after excluding the contribution from redshift uncertainty and sightline-to-sightline variance. None the less, the transmitted flux values of the control sample might be correlated because of the overlap in the comparison samples for quasars at similar emission redshifts. We mitigated such correlations by exclusion bootstrapping, viz. by randomly retaining only one sightline out of the total five sightlines used as a control sample for each sightline of the proximity region, and generated 100 such realizations. The distribution of the transmitted flux in each radial bin is found to be Gaussian. The width of this Gaussian distribution is then added to the error budget of IGM. Moreover, the sample size of the control sample is typically five times larger than the proximity sample (due to our choice of five control samples for each main sample), which results in much smaller statistical errors.

3.4 Transmitted flux statistics

We have plotted in Fig. 4 median values of $F_{\rm t}$ within various 2-Mpc radial distance bins, towards and away from the quasars. The negative distances in the x-axis are just sign convention used in equation (3) to represent the absorbing clouds present in the vicinity of the main quasars towards the observer. The grey shades show the median redshift of the pixels contributing to each of the radial distance bin.

A first noticeable point from Fig. 4 is that the $F_{\rm t}$ measured at large radial distances from the quasar (i.e. ≥14 Mpc) is consistent with that from the IGM obtained using the control sample (as expected). For each radial distance bin, we have combined all the pixels based on their distances from the quasar falling within that radial bin, but these pixels have absorption redshift spread over a large range. This can result in a gradual slope in the transmitted flux with radial distance for the Ly α absorbers as the median absorption redshift of the pixels in a given radial distance bin decreases towards the observer (e.g. see redshift-based grey shade in Fig. 4). However, we reiterate that our selection of the control samples (see e.g. Section 2.2) with exact matching in absorption redshift takes care of such effects due to the similar redshift evolution expected. This is also evident from the similarity of redshift depicted by grey shade for both the IGM and the proximity region.

From Fig. 4, it can be seen that the proximity effect is significant up to a distance of 12 Mpc with a clear increase in the transmitted flux ($F_{\rm t}$) as we go closer to the quasar as expected in the classical proximity effect. Also, in the region redward of the quasars $F_{\rm t} \sim 1$, which is expected as it represents the continuum region. The consistency of $F_{\rm t} \sim 1$ can be noticed even in the first radial bin redward of quasars. This indicates that the possible uncertainty in the redshift estimation (as given by López et al. 2016) due to any peculiar motion (if any) is not significant at scales ≥2 Mpc.

3.5 Median pixel optical depth profile around the quasar

3.5.1 Degeneracy between ionization and excess optical depth at moderate resolution

To lift the degeneracy between the effect of excess ionization from the quasars and the presence of excess pixel optical depth ratio around the quasar in comparison to the IGM, we follow the procedure as detailed in JCS19, with a brief discussion given below. Here, we make use of the UVB measurements from Khaire & Srianand (2015a, 2019) based on an independent method using updated comoving specific emissivities of galaxies and quasars at different frequencies (from UV to FIR) and redshifts. The combined effect leads to shift in the observed pixel optical depth in the proximity region $\tau_{\rm p}$ (e.g. see JCS19 and references therein) as would have been expected in the IGM ($\tau_{\rm IGM}$),

$$\tau_{\rm IGM} = \tau_{\rm p}\,\frac{\left[1+\omega_{\rm r}^{\rm ef}(\tau_{\rm p},\omega_{\rm r})\right]}{(\rho(r)/\bar{\rho}_{\rm IGM})^{\beta}} \tag{6}$$

leading to

$$\left[\frac{\rho(r)}{\bar{\rho}_{\rm IGM}}\right]^{\beta} = \frac{\tau_{\rm p}\times\left[1+\omega_{\rm r}^{\rm ef}(\tau_{\rm p},\omega_{\rm r})\right]}{\tau_{\rm IGM}} \tag{7}$$

with $\beta \equiv 2 - 0.7(\gamma - 1)$, with γ representing the slope of the temperature (T)–density (Δ) relation viz., $T = T_{\rm o}\Delta^{\gamma-1}$. Here, $\tau_{\rm p}$ (or $\tau_{\rm p}[\lambda_i]$) is the measured pixel optical depth in the presence of the quasar and $\tau_{\rm IGM}$ is the expected pixel optical depth from the IGM, which we have estimated using the absorption redshift matched control sample. The term $\tau_{\rm p}\times[1+\omega_{\rm r}^{\rm ef}(\tau,\omega_{\rm r})]/\tau_{\rm IGM}$ represents the ratio of the pixel optical depth corrected for quasar's ionization in the proximity region to that of the pixel optical depth of the general IGM. We have estimated this ratio within a radial bin of 1 Mpc by taking median value, i.e.

$$\frac{\rm Median(\tau_{\rm p}\times\left[1+\omega_{\rm r}^{\rm ef}(\tau,\omega_{\rm r})\right])}{\rm Median(\tau_{\rm IGM})} \equiv R_{\tau}(r). \tag{8}$$

This will be the manifestation of the excess overdensity around the quasars (e.g. see equation 7) in the radial bin where $R_{\tau}(r)$ is more than unity, though the mapping between $R_{\tau}(r)$ and overdensity might require proper calibration using detailed numerical simulations.

The $[1+\omega_{\rm r}^{\rm ef}]$ is equivalent of $[1+\omega_{\rm r}]$ ionization scaling of $\tau_{\rm p}$ after taking into account the effect of moderate spectral resolution ($R\sim5100$) and pixel optical depth value where $[1+\omega_{\rm r}]$ is defined as,

$$\frac{\Gamma_{\rm UVB}(z_{\rm a})+\Gamma_{\rm q}(r,z_{\rm a})}{\Gamma_{\rm UVB}(z_{\rm a})} \equiv 1+\omega_{\rm r} \tag{9}$$

with $\Gamma_{\rm UVB}(z_{\rm a})$ (taken from Khaire & Srianand 2015a, 2019) and $\Gamma_{\rm q}(r, z_{\rm a})$ being the H I photoionization rates at the absorption redshift $z_{\rm a}$ contributed by the UVB and quasar, respectively.

In Fig. 5, we show the departure of the effective ionization correction parameter, $[\Gamma_{\rm q}/\Gamma_{\rm UVB}]^{\rm ef}(\equiv\omega_{\rm r}^{\rm ef}(\tau,\omega_{\rm r}))$, from its theoretical value of $\Gamma_{\rm q}/\Gamma_{\rm UVB}(\equiv\omega_{\rm r})$ in various pixel optical depth bins at spectral resolution of ∼5100 (the typical resolution of our X-SHOOTER spectra). Here, the $\omega_{\rm r}$ is used to vary the level of ionization in the simulated IGM spectra (Gaikwad et al. 2018), with pixel optical depth $\tau_{\rm true}$ as $\tau_{\rm true}/[1+\omega_{\rm r}]$. The transmitted flux corresponding to $\tau_{\rm true}$ and $\tau_{\rm true}/[1+\omega_{\rm r}]$ is convolved with Gaussian kernel corresponding to the X-SHOOTER resolution to obtain transmitted flux leading to simulated pixel optical depths $\tau_{\rm IGM}$ and $\tau_{\rm p}$, respectively. The best fit is computed such that KS-test probability is maximum for the distribution of $\tau_{\rm p}\times[1+\omega_{\rm r}^{\rm ef}(\tau,\omega_{\rm r})]$ and distribution of $\tau_{\rm IGM}$ to be similar at each optical depth bin of $\tau_{\rm p}$, as detailed in JCS19. In the hydrodynamical simulation of IGM used here from Gaikwad et al. (2018), they have used GADGET-3 simulation[4], with box size of $10\,h^{-1}$ cMpc having 2×512^3 number of particles and mass resolution of $\sim10^5\,h^{-1}\,M_{\odot}$. The UVB used in this simulation was given by Haardt & Madau (2012). We note that the UVB used in our analysis (i.e. Khaire & Srianand 2015a, 2019) is different from the UVB model used in the simulations (Haardt & Madau 2012). This replacement of the UVB model may alter the overall optical depth distribution of simulated IGM. However, it will not have any significant impact on the above $\omega_{\rm r}$ and $\omega_{\rm r}^{\rm ef}$ relation, as we have used here the simulations only to calibrate the ionization correction at a given pixel optical depth (using small bins of optical depth, e.g. see Fig. 5), which will not have any significant dependence on the overall distribution of the optical depth.

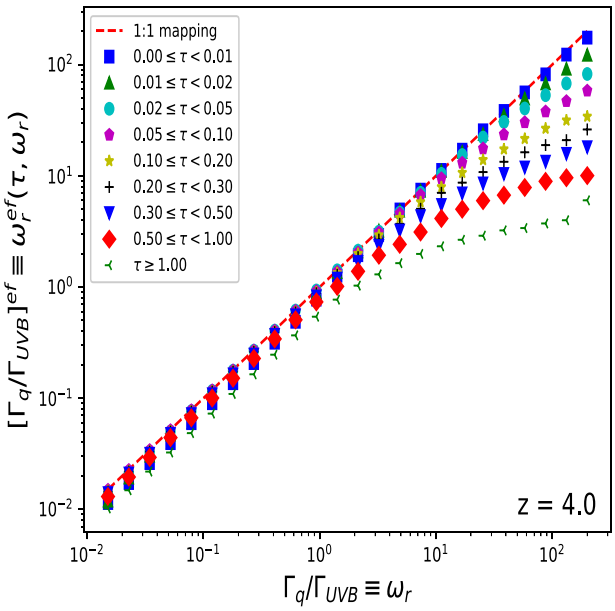

Figure 5. The plot shows the departure of the effective ionization correction parameter, $[\Gamma_{\rm q}/\Gamma_{\rm UVB}]^{\rm ef}(\equiv\omega_{\rm r}^{\rm ef}(\tau,\omega_{\rm r}))$, from its theoretical value of $\Gamma_{\rm q}/\Gamma_{\rm UVB}(\equiv\omega_{\rm r})$ in various pixel optical depth bins (listed in inset) obtained for spectra generated with a resolution mimicking the X-SHOOTER observations.

It is evident from Fig. 5 that there is a significant departure of $\omega_{\rm r}^{\rm ef}(\tau,\omega_{\rm r})$ from $\omega_{\rm r}$ at least for higher optical depth bins and higher values of $\omega_{\rm r}$.

3.5.2 Pixel optical depth statistics

In our further analysis, we calculate the pixel optical depth values (integrated value over the pixel width of ∼20 km s^{-1}) from the transmitted flux $F_{\rm t}(\lambda_i)$ as used in the Fig. 4; the binning is, however, reduced to 1 Mpc. We plot in the right-hand panel of Fig. 6 the 'ratio of median pixel optical depth (i.e. $R_{\tau}(r)$)' in each 1-Mpc radial bin. The errors are then propagated appropriately as discussed in Section 3.3 from each pixel to a given radial distance bin of 1 Mpc. The plot shows that the ratio of median pixel optical depth increases with a decrease in the radial distance r with a significant excess in the range of $-6\le r\le0$ Mpc. In addition to these errors, uncertainty

[4]http://wwwmpa.mpa-garching.mpg.de/gadget/

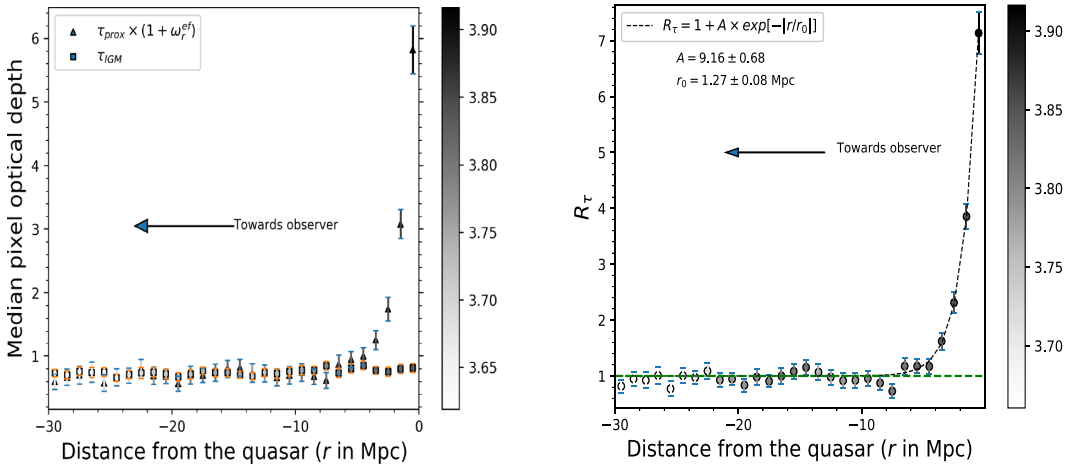

Figure 6. *Left-hand panel*: The plot shows the median pixel optical depth corrected for quasar's ionization in the proximity region (triangle) and the median pixel optical depth of the general IGM (square) at different radial distance bin of 1 Mpc. The grey shades represent the median value of the absorption redshifts (along the proximity sightline) in each radial distance bin. The resultant error bars consist of the flux error from photon-counting statistics, redshift uncertainty, sightline-to-sightline variance, and rms statistical error within the 1-Mpc radial distance bin as also used in Fig. 4 along with the error propagation in $[1+\omega_r^{ef}(\tau,\omega_r)]$ based on the uncertainty in the pixel optical depth. *Right-hand panel*: The plot shows the ratio of median pixel optical depth shown as two curves in the left-hand panel (defined as $R_\tau(r)$ in equations 7 and 8) in a radial distance bin of 1 Mpc.

in the $\omega_r^{ef}(\tau,\omega_r)$ due to measurement uncertainty in τ is also taken into account, as,

$$|\omega_r^{ef}(\tau+\Delta\tau)-\omega_r^{ef}(\tau-\Delta\tau)|/2. \quad (10)$$

In order to quantify the radial extents around the quasars, where the $R_\tau(r)$ is significantly higher than unity, we parametrize the $R_\tau(r)$ versus r curve by a fitting function of the form $R_\tau(r) = 1 + A \times \exp(-r/r_0)$. The best-fitting parameters are determined by using the χ^2 fit, resulting in $A = 9.16 \pm 0.68$ and $r_0 = 1.27 \pm 0.08$ Mpc. The best-fitting profile is shown in the right-hand panel of Fig. 6, which deviates from the unity with $\geq 1\sigma$ for region $-6\,\mathrm{Mpc} \leq r \leq 0$ (proper), with σ being the median value of error bar on $R_\tau(r)$. In this 6-Mpc region, the integrated value of scaled pixel optical depth (i.e. $\tau_p \times [1+\omega_r^{ef}(\tau,\omega_r)]$ by triangles in left-hand panel of Fig. 6) is found to be higher by a factor of 2.55 ± 0.17 in comparison to the corresponding integrated value of the τ_{IGM} curve (shown by squares in left-hand panel of Fig. 6). Here, the estimated uncertainty is computed based on the proper error propagation (assuming Gaussian in nature) from the individual error bar as shown in the left-hand panel of Fig. 6. We also used the Kolmogorov–Smirnov test (KS test) and found that the null probability for the distribution of $\tau_p \times [1+\omega_r^{ef}(\tau,\omega_r)]$ and τ_{IGM} within 6 Mpc to belong to same distribution is ruled out at 100 per cent confidence level.

4 RESULTS AND DISCUSSIONS

Studies in the past have established that quasars reside in an overdense gaseous environment based on various techniques such as clustering analysis, cross-correlation, etc. (e.g. see White et al. 2012; Trainor & Steidel 2013). Here, we have used a novel technique from our recent study in JCS19 to estimate the ratio of median pixel optical depth [i.e. $R_\tau(r)$] profile surrounding the high-redshift quasars based on the longitudinal proximity effect. The procedure involves the analysis of the proximity effect using the existing measurements of UVB leading to an estimate of the $R_\tau(r)$ profile around the quasar. The noticeable point in our analysis is that it takes care of the redshift evolution of the pixel optical depth using a control sample matched in absorption redshift along with similarity in S/N. This procedure surpasses the method of scaling the pixel optical depth to a reference redshift. The latter has a caveat of scaling continuum noise pixels as well as problematic for the saturated pixels. Additionally, our study also takes into account the effect of the spectral resolution and pixel optical depth while correcting for the effect of quasar's ionization.

The sample used in this study consists of 85 quasars from the XQ-100 survey covering a redshift range from 3.5 to 4.5. These quasars have Lyman continuum luminosity in the range of 1.06×10^{31} to 2.24×10^{32} erg s^{-1} Hz^{-1} (e.g. see Fig. 1) with spectral resolution of $R \sim 5100$ and $S/N \sim 30$ (e.g. see Section 2). We find the presence of the proximity effect up to a proper distance of 12 Mpc (e.g. see Fig. 4). It can be noted from Fig. 6 right-hand panel that the ratio of median pixel optical depth is found to be higher than unity in the region of $-6 \leq r \leq 0$ Mpc (proper) in the vicinity of the quasar. The integrated value of $\tau_p \times [1+\omega_r^{ef}(\tau,\omega_r)]$ (shown by triangle in the left-hand panel of Fig. 6) in the $-6 \leq r \leq 0$ region is found to be higher by a factor of 2.55 ± 0.17 than that of the corresponding integrated value of τ_{IGM} (shown by square in the left-hand panel of Fig. 6).

In our analysis, we have assumed a single value of the spectral index (α) for all the sources. However, previous studies have reported a range of values for the spectral indexes. For example, Stevans et al. (2014) estimated $\alpha = 0.83 \pm 0.09$ for 1200–2000 Å (rest frame) and $\alpha = 1.41 \pm 0.15$ for 500–1000 Å for the composite spectrum obtained by *Hubble Space Telescope*. Similarly, Lusso et al. (2015) analysis estimates far-ultraviolet spectral index $\alpha = 0.61 \pm 0.01$ and at shorter wavelengths $\alpha = 1.70 \pm 0.61$. As pointed out in Section 2.1, in our previous work (JCS19), we have shown that the impact of dispersion of the UV-spectral index is negligible as far as $R_\tau(r)$ is concerned. Similar to JCS19, we have re-estimated our ratio of median pixel optical depth profile using two extreme values of UV-spectral index, viz. 1.96 and 0.56. We found similar $R_\tau(r)$ profile as shown in the right-hand panel of Fig. 6. In the distance range of -6

$\leq r \leq 0$ Mpc, the integrated value of $\tau_p \times [1 + \omega_r^{ef}(\tau, \omega_r)]$ if found to be higher than integrated value of τ_{IGM} by a factor of 2.28 ± 0.16 and 3.42 ± 0.20 for $\alpha = 1.96$ and $\alpha = 0.56$, respectively.

We also note that though in the visual check the continuum fit given by López et al. (2016) seems to be very robust, at high redshifts, the crowding of Ly α absorption can lead to no absorption-free region in the Ly α forest. In this scenario, the best-fitting continuum may be underestimated. In order to take into account the effect of such continuum underestimation, we also apply a systematic continuum shift based on the analysis of Faucher-Giguère et al. (2008b, see e.g. Section 3.1). However, we also repeated the analysis of median transmitted flux (i.e. Fig. 4) and median pixel optical depth (i.e. Fig. 6) without applying such continuum shift. We found that the proximity effect is still evident up to a distance of 12 Mpc and the ratio of median pixel optical depth is significantly higher than unity in the $-5 \leq r \leq 0$ Mpc.

We also note that in our recent work, JCS19, we have estimated the $R_\tau(r)$ in the longitudinal direction using 181 quasar pairs from SDSS (relatively smaller spectral resolution, $R \sim 2000$ and $S/N \sim 10$) sample using the same technique. The longitudinal proximity effect and the $R_\tau(r)$ in that study were found significant up to 4 Mpc. The extent and the significance level of the detection are comparatively much higher in the present study perhaps due to the higher quality quasar spectra used ($R \sim 5100$ and $S/N \sim 30$) and/or probably due to higher redshift and luminosity of the quasars in the sample used here.

Such proximity effect is also reported by many of the previous studies. For example, Guimarães et al. (2007) also used quasars with a similar redshift range (i.e. $z_{em} > 4$) and found evidence for the proximity effect to a distance of $r \sim 15-20$ Mpc. However, in their analysis, while correcting for quasar's ionization, they have not considered its dependence on the spectral resolution and pixel optical depth as we have done in our analysis (e.g. see Section 3.5). Similarly, Calverley et al. (2011) found proximity effect evident from 3 Mpc to 10 Mpc at the redshift range from 4.5 to 6.5. Here, a tentative increase evident in the extent of the proximity region with an increase in the average emission redshift of the sample could be due to bias in selecting higher luminosity quasars at higher redshifts (see also Eilers et al. 2017).

Similarly, in the context of our result that $R_\tau(r) > 1$ for $-6 \leq r \leq 0$ Mpc, which could be the manifestation of the excess overdensity around quasar, we note that Scott et al. (2000) found the excess overdensity within 1.5 h^{-1} Mpc at 5.5σ level. Rollinde et al. (2005) claimed detection of overdensities of about a factor of 2 on scales $\sim$5 Mpc for quasars at redshift $z \sim 2$. Similarly, Guimarães et al. (2007) reported an excess overdensity of the order of 2 on the scales of $\sim$10 Mpc. A small minority of quasars in Dall'Aglio, Wisotzki & Worseck (2008a) shows substantial overdensities of up to a factor of a few, till 3 Mpc. Furthermore, D'Odorico et al. (2008) found excess overdensity in the region within 4 Mpc from the quasar's position. The main improvement in our present study of the ratio of median pixel optical depth study is that while applying the correction for the excess ionization of the quasar, we have taken into account the effect of spectral resolution and the pixel optical depth dependence.

Our result that $R_\tau(r) > 1$ is also consistent with the fact that in order to form structures in the universe, the collapsed regions should have a mean density higher than its critical value to overcome the Hubble flow (e.g. see Loeb & Eisenstein 1995; Rollinde et al. 2005). The halo profiles grow via the infall of matter towards their centres and it can extend to a radius much greater than the virial radius (e.g. see Faucher-Giguère et al. 2008a, and references therein). Therefore, the absorbing gas is not at rest with respect to the quasar centre resulting in non-zero peculiar velocities. Faucher-Giguère et al. (2008a) showed that this peculiar velocity shifts the absorption redshift of the gas parcel through the Doppler effect and it is much significant compared to the thermal motion of the gas particles. Additionally, Hui, Gnedin & Zhang (1997) showed from their analysis that these peculiar velocities play an important role in determining the absorption profiles but their effect on the column density distribution is minor. It may be recalled that in our result of excess pixel optical depth profile as shown in Fig. 6, all possible sources of errors have been considered except the possible impact of the aforementioned peculiar velocity. Using a first-order approximation as explained in Faucher-Giguère et al. (2008a), an in-falling gas parcel will absorb radiation that has Ly α frequency (in the quasar rest frame) at proper distance $r' = r - \Delta r$ from the quasar, where $\Delta r = v_{\parallel}/H(z)$ with $v_{\parallel}$ representing peculiar velocity (<0 for motion in-falling towards the quasar). Assuming the peculiar velocity to be as significant as Hubble flow, i.e. $v_{\parallel} \sim -420$ km s^{-1} at $<z_{em}> = 4$, we obtain $|\Delta r| = 1$ Mpc. Therefore, although there could be a dilution of the magnitude of the measured value of $R_\tau(r)$ due to this peculiar velocity, its impact due to $\geq$1-Mpc binning in our analysis may not be significant as far as the excess pixel optical depth ratio profile is concerned. However, in a realistic situation, outflow also exists in the vicinity of the quasar, which can lead to the dilution of any such impact of inflow. Furthermore, as we pointed out in Section 3.4, the transmitted flux as shown in Fig. 4 shows a sharp transition without the wing in the transition from the blue side (i.e. proximity region) to the redward side of the quasars emission line centroid, suggesting a minor effect of peculiar velocity in our analysis. However, it will be important to quantify how the derived density profile will be modified if we include the peculiar velocities using cosmological simulations.

Moreover, the $R_\tau(r)$ is also expected to be correlated with the quasar's luminosity, i.e. brighter quasars may live in a region of higher overdensities (e.g. see Guimarães et al. 2007, and references therein). In order to check this effect, we devised a subsample of low and high luminosity. In the low- and high-luminosity bins, we have taken 25 lowest and 25 highest ($\sim$29 per cent of the total sample) luminosity quasars of our sample. As can be seen from Fig. 7, the excess pixel optical depth ratio is more pronounced for the subsample of higher luminosity with $<\log L_{912}> = 31.85$ ergs s^{-1} Hz^{-1} as compared to the subsample of lower luminosity with $<\log L_{912}> = 31.12$ ergs s^{-1} Hz^{-1}. The integrated value under the $\tau_p \times [1 + \omega_r^{ef}(\tau, \omega_r)]$ curve (e.g. see Fig. 7) between $-6 \leq r \leq 0$ Mpc is found to be higher by a factor of 3.70 ± 0.22 and 1.62 ± 0.15 w.r.t. the corresponding integrated value of τ_{IGM} curve for high- and low-luminosity subsamples, respectively. However, we do notice that higher luminosity bin has a higher median redshift of $<z_{em}> = 4.06$ in comparison to $<z_{em}> = 3.85$ for the lower luminosity bin (e.g. see grey shade). However, the above $R_\tau(r)$ difference, especially in the $-2 \leq r \leq 0$ Mpc bins, cannot be merely explained by the redshift difference in these two subsamples.

Additionally, we also used our sample to check for any difference of density profile among radio-loud (RL) and radio-quiet (RQ) quasars (e.g. see Sopp & Alexander 1991; Dunlop et al. 2003; Gopal-Krishna, Mangalam & Wiita 2008; Retana-Montenegro & Röttgering 2017) where the former is generally associated with the presence of jets. Such bimodality is quantified by a radio-loudness parameter (*i.e.* $\mathcal{R}$) defined as a ratio between the rest-frame flux densities at 5 GHz and 2500 Å (see also Ivezić et al. 2002; Kellermann et al. 2016, and references therein), with its value $\mathcal{R} \geq 23$ for RL sources

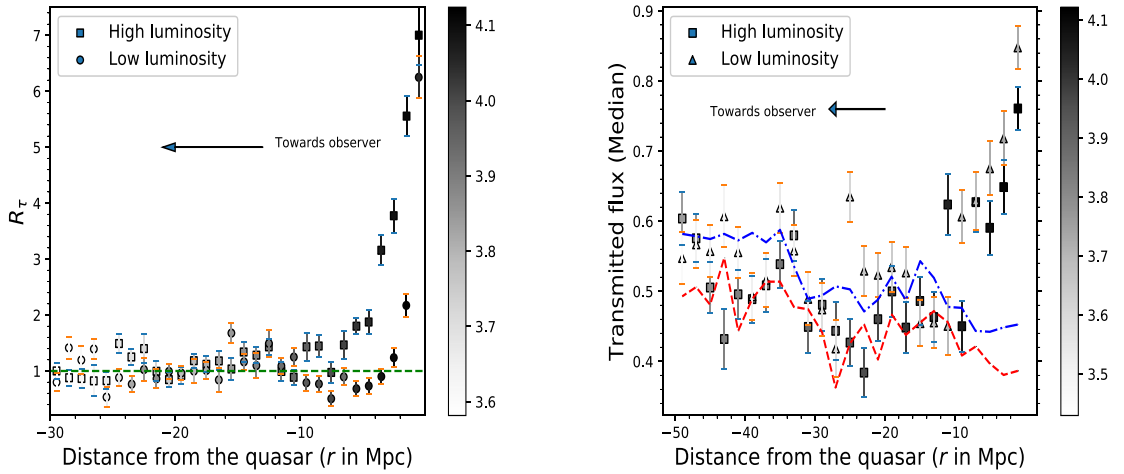

Figure 7. *Left-hand panel*: Same as right-hand panel of Fig. 6, but for the extreme 25 low- and 25 high-luminosity quasars in our sample (e.g. see text in Section 4). The Lyman continuum luminosity was calculated using V-band magnitude (e.g. see Section 2.1.) *Right-hand panel*: The plot shows radius versus flux (similar to Fig. 4) for the transmitted flux of the subsample of extreme 25 low- and 25 high-luminosity quasars. The transmitted flux of the control sample of IGM for the higher luminosity and lower luminosity quasars is shown in red-dashed and blue dot–dashed lines, respectively.

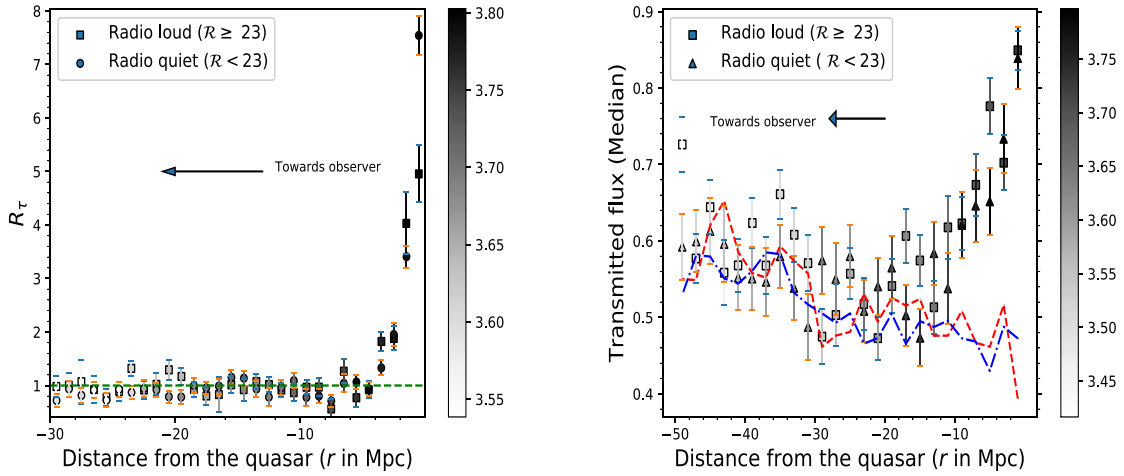

Figure 8. *Left-hand panel*: Same as right-hand panel of Fig. 6, but for the RL (total 12 quasars with $\mathcal{R} \geq 23$) and for the RQ (total 50 quasars with $\mathcal{R} < 23$) quasars in our sample. The radio-loudness parameter ($\mathcal{R}$) was taken from Perrotta et al. (2016). *Right-hand panel*: Same as right-hand panel of Fig. 7, but for the RL and RQ subsample of quasars. The transmitted flux from the control sample of IGM for RL and RQ quasars is shown in red-dashed and blue dot–dashed lines, respectively.

as adopted by Ganguly et al. (2013). Out of the 85 quasars in our sample, 62 have information about its radio-loudness parameter with 12 being RL (i.e. $\mathcal{R} \geq 23$) quasars and 50 being RQ (i.e. $\mathcal{R} < 23$) quasars (e.g. see Perrotta et al. 2016). We plot $R_\tau(r)$ for these two sub-samples (i.e. RL and RQ quasars) as shown in Fig. 8. From this figure, it is evident that their $R_\tau(r)$ profile is quite similar in both sub-samples, though the sample size of RL quasars is small here (12 quasars). Here, we also note that the typical luminosity (median) among these two sub-samples is almost similar being 2.23×10^{31} erg s^{-1} Hz^{-1} and 1.55×10^{31} erg s^{-1} Hz^{-1} for the former and the latter, respectively.

To summarize, our sample of 85 quasars from XQ-100 survey based on X-SHOOTER observations at high R ($\sim$5100) and high *S/N* ($\sim$30) has allowed us to constrain the ratio of median pixel optical depth profile for quasar in redshift range from 3.5 to 4.5 and luminosity range from 1.06×10^{31} to 2.24×10^{32} erg s^{-1} Hz^{-1}. Here, while correcting for quasar's ionization, we have properly taken into account the effect of spectral resolution and pixel optical depth using detailed simulations. The ratio of median pixel optical depth is found to be significant up to 6 Mpc. The area under the curve of $\tau_p \times [1 + \omega_r^{ef}(\tau, \omega_r)]$ over 0–6 Mpc range is found to be higher by a factor of 2.55 ± 0.17 in comparison to the corresponding area under τ_{IGM} verses r curve. The KS test ruled out the null probability of $\tau_p \times [1 + \omega_r^{ef}(\tau, \omega_r)]$ and τ_{IGM} within 6 Mpc to belong to same distribution at 100 per cent confidence level. This excess factor for subsample with average luminosity $<\log L_{912}> = 31.85$ (at $<z_{em}> = 4.06$), and $<\log L_{912}> = 31.12$ (at $<z_{em}> = 3.85$), is found to be 3.70 ± 0.22 and 1.62 ± 0.15, respectively, suggesting its dependence on luminosity.

Further improvement to constrain the ratio of median pixel optical depth profile and its dependence on various parameters such as luminosity, redshift, and radio-loudness will require a much larger sample size from future spectroscopic surveys with high-quality data as is used here from XQ-100 survey.

ACKNOWLEDGEMENTS

The authors thank the anonymous referee for his or her valuable comments/suggestions that have improved the manuscript. The authors would also like to thank Dr. Sarah Bosman for the discussion regarding continuum uncertainties. The authors acknowledge Dr. Prakash Gaikwad and Dr. Vikram Khaire for providing the simulated IGM spectra at $<z> = 4$ and the latest value of UV-background radiation, respectively. The authors also like to thank the XQ-100 team for providing access to the processed data publicly available, based on observations made with ESO Telescopes at the La Silla or Paranal Observatories under programme ID(s) 189.A-0424(A) and 189.A-0424(B).

DATA AVAILABILITY

Based on observations made with ESO Telescopes at the La Silla or Paranal Observatories under programme ID(s) 189.A-0424(A) and 189.A-0424(B). The data used in this article are available at: http://archive.eso.org/wdb/wdb/adp/phase3_main/form as provided by López et al. (2016).

REFERENCES

Adelberger K. L., 2004, ApJ, 612, 706
Bajtlik S., Duncan R. C., Ostriker J. P., 1988, ApJ, 327, 570
Bechtold J., 1994, ApJS, 91, 1
Becker G. D., Rauch M., Sargent W. L. W., 2007, ApJ, 662, 72
Becker G. D., Hewett P. C., Worseck G., Prochaska J. X., 2013, MNRAS, 430, 2067
Becker G. D., Bolton J. S., Lidz A., 2015, PASA, 32, e045
Bennett C. L., Larson D., Weiland J. L., Hinshaw G., 2014, ApJ, 794, 135
Berg T. A. M. et al., 2019, MNRAS, 488, 4356
Calverley A. P., Becker G. D., Haehnelt M. G., Bolton J. S., 2011, MNRAS, 412, 2543
Carswell R. F., Whelan J. A. J., Smith M. G., Boksenberg A., Tytler D., 1982, MNRAS, 198, 91
Clayton G. C., Cardelli J. A., 1988, AJ, 96, 695
Cooke A. J., Espey B., Carswell R. F., 1997, MNRAS, 284, 552
Cristiani S., Vio R., 1990, A&A, 227, 385
D'Odorico V., Bruscoli M., Saitta F., Fontanot F., Viel M., Cristiani S., Monaco P., 2008, MNRAS, 389, 1727
Dall'Aglio A., Wisotzki L., Worseck G., 2008a, A&A, 491, 465
Dall'Aglio A., Wisotzki L., Worseck G., 2008b, A&A, 480, 359
Denney K. D. et al., 2016, ApJS, 224, 14
Dix C., Shemmer O., Brotherton M. S., Green R. F., Mason M., Myers A. D., 2020, ApJ, 893, 14
Drake A. J. et al., 2009, ApJ, 696, 870
Dunlop J. S., McLure R. J., Kukula M. J., Baum S. A., O'Dea C. P., Hughes D. H., 2003, MNRAS, 340, 1095
Efron B., Tibshirani J. R., 1993, An Introduction to the Bootstrap. Chapman & Hall/CRC, UK
Eilers A.-C., Davies F. B., Hennawi J. F., Prochaska J. X., Lukić Z., Mazzucchelli C., 2017, ApJ, 840, 24
Faucher-Giguère C.-A., Lidz A., Zaldarriaga M., Hernquist L., 2008a, ApJ, 673, 39
Faucher-Giguère C.-A., Prochaska J. X., Lidz A., Hernquist L., Zaldarriaga M., 2008b, ApJ, 681, 831
Faucher-Giguère C.-A., Lidz A., Zaldarriaga M., Hernquist L., 2009, ApJ, 703, 1416
Gaikwad P., Choudhury T. R., Srianand R., Khaire V., 2018, MNRAS, 474, 2233
Gallerani S., 2011, J. Phys. Conf. Ser., 280, 012008
Ganguly R. et al., 2013, MNRAS, 435, 1233
Giallongo E., 1991, MNRAS, 251, 541
Giallongo E., Cristiani S., D'Odorico S., Fontana A., Savaglio S., 1996, ApJ, 466, 46
Gonçalves T. S., Steidel C. C., Pettini M., 2008, ApJ, 676, 816
Gopal-Krishna, Mangalam A., Wiita P. J., 2008, ApJ, 680, L13
Guimarães R., Petitjean P., Rollinde E., de Carvalho R. R., Djorgovski S. G., Srianand R., Aghaee A., Castro S., 2007, MNRAS, 377, 657
Haardt F., Madau P., 2012, ApJ, 746, 125
Hennawi J. F., Prochaska J. X., 2013, ApJ, 766, 58
Hui L., Gnedin N. Y., Zhang Y., 1997, ApJ, 486, 599
Ivezić Ž. et al., 2002, AJ, 124, 2364
Jalan P., Chand H., Srianand R., 2019, ApJ, 884, 151
Johnson H. L., Morgan W. W., 1951, ApJ, 114, 522
Kellermann K. I., Condon J. J., Kimball A. E., Perley R. A., Ivezić Ž., 2016, ApJ, 831, 168
Khaire V., Srianand R., 2015a, MNRAS, 451, L30
Khaire V., Srianand R., 2015b, ApJ, 805, 33
Khaire V., Srianand R., 2019, MNRAS, 484, 4174
Khrykin I. S., Hennawi J. F., McQuinn M., Worseck G., 2016, ApJ, 824, 133
Kim T. S., Bolton J. S., Viel M., Haehnelt M. G., Carswell R. F., 2007, MNRAS, 382, 1657
Kim T. S., Carswell R. F., Mongardi C., Partl A. M., Mücket J. P., Barai P., Cristiani S., 2016, MNRAS, 457, 2005
Kirkman D., Tytler D., 2008, MNRAS, 391, 1457
Kulkarni V. P., Fall S. M., 1993, ApJ, 413, L63
Lau M. W., Prochaska J. X., Hennawi J. F., 2016, ApJS, 226, 25
Lau M. W., Prochaska J. X., Hennawi J. F., 2018, ApJ, 857, 126
Lidz A., Heitmann K., Hui L., Habib S., Rauch M., Sargent W. L. W., 2006, ApJ, 638, 27
Liske J., Williger G. M., 2001, MNRAS, 328, 653
Loeb A., Eisenstein D. J., 1995, ApJ, 448, 17
López S. et al., 2016, A&A, 594, A91
Lu L., Wolfe A. M., Turnshek D. A., 1991, ApJ, 367, 19
Lusso E., Worseck G., Hennawi J. F., Prochaska J. X., Vignali C., Stern J., O'Meara J. M., 2015, MNRAS, 449, 4204
Monzon J. S., Prochaska J. X., Lee K.-G., Chisholm J., 2020, AJ, 160, 37
Murdoch H. S., Hunstead R. W., Pettini M., Blades J. C., 1986, ApJ, 309, 19
Pâris I. et al., 2017, A&A, 597, A79
Partl A. M., Müller V., Yepes G., Gottlöber S., 2011, MNRAS, 415, 3851
Perrotta S. et al., 2016, MNRAS, 462, 3285
Prochaska J. X. et al., 2013, ApJ, 776, 136
Prochaska J. X., Lau M. W., Hennawi J. F., 2014, ApJ, 796, 140
Retana-Montenegro E., Röttgering H. J. A., 2017, A&A, 600, A97
Rollinde E., Srianand R., Theuns T., Petitjean P., Chand H., 2005, MNRAS, 361, 1015
Sánchez-Ramírez R. et al., 2016, MNRAS, 456, 4488
Schirber M., Miralda-Escudé J., McDonald P., 2004, ApJ, 610, 105
Schlegel D. J., Finkbeiner D. P., Davis M., 1998, ApJ, 500, 525
Schmidt T. M., Hennawi J. F., Worseck G., Davies F. B., Lukić Z., Oñorbe J., 2018, ApJ, 861, 122
Scott J., Bechtold J., Dobrzycki A., Kulkarni V. P., 2000, ApJS, 130, 67
Seljak U., McDonald P., Makarov A., 2003, MNRAS, 342, L79
Shen Y. et al., 2016, ApJ, 831, 7
Sopp H. M., Alexander P., 1991, MNRAS, 251, 112
Srianand R., 1997, ApJ, 478, 511
Srianand R., Khare P., 1996, MNRAS, 280, 767
Stevans M. L., Shull J. M., Danforth C. W., Tilton E. M., 2014, ApJ, 794, 75

Telfer R. C., Zheng W., Kriss G. A., Davidsen A. F., 2002, ApJ, 565, 773
Trainor R., Steidel C. C., 2013, ApJ, 775, L3
Tytler D., 1987, ApJ, 321, 69
Vanden Berk D. E. et al., 2001, AJ, 122, 549
Vernet J. et al., 2011, A&A, 536, A105
Walther M., Hennawi J. F., Hiss H., Oñorbe J., Lee K.-G., Rorai A., O'Meara J., 2018, ApJ, 852, 22
White M. et al., 2012, MNRAS, 424, 933
Wild V. et al., 2008, MNRAS, 388, 227
Worseck G., Wisotzki L., 2006, A&A, 450, 495
Worseck G., Fechner C., Wisotzki L., Dall'Aglio A., 2007, A&A, 473, 805

SUPPORTING INFORMATION

Supplementary data are available at *MNRAS* online.

Table 1. Some properties of 100 quasars used in our analysis with masked absorption redshifts.

Please note: Oxford University Press is not responsible for the content or functionality of any supporting materials supplied by the authors. Any queries (other than missing material) should be directed to the corresponding author for the article.

This paper has been typeset from a TEX/LATEX file prepared by the author.